ORIGINAL RESEARCH ARTICLE

Study on Construction Mechanism of Ceramic–Metal Thermal Barrier Coating System by Plasma Spraying

JUNYI XIAO, JIAJING PAN, YU GU, HAITAO LU, NAN YU, MINGLI LV, and XIAOLIN CHEN

A unique construction mechanism is present in the plasma-spraying process of the ceramic–metal thermal barrier coating (TBC) system. This study combines experimental and simulation methods for investigating the mechanism of how three ceramic–metal TBC systems (Y_2O_3-MCrAlY, 8YSZ-MCrAlY, and Cr_2O_3-Ni20Cr) are constructed on Inconel718 alloy substrates. The three systems are bilayer coatings with a ceramic as the top coat (TC) and metal as the bond coat (BC). The coatings have different morphologies depending on the degree of softening, and substrate BC is more likely to achieve a higher metallurgical bond than TC–BC. The property differences between BC and TC may affect the bonding strength of the TBC systems. In constructing bilayer coatings, the temperature and equivalent stress of coating particles are related to their own thermal conductivity and thermal softening coefficient, respectively. In addition, constructing the TC is the main factor that causes the temperature effects, and constructing the BC is the main factor that causes the equivalent stress effects. Furthermore, the constructed BC first protects the substrate and reduces the influence of the TC that is later constructed on the substrate. This study provides a basic reference for relevant engineering applications and subsequent in-depth research on bilayer and multilayer coating systems.

I. INTRODUCTION

MANY components in modern industrial machinery, such as gears and turbine blades, are exposed to harsh thermal environments that include high temperatures, thermal oxidation, and thermal corrosion.[1] To overcome the environmental challenges and to further improve the performance of the equipment, TBCs are constructed that have the functions of thermal oxidation resistance, thermal conductivity resistance, and thermal corrosion resistance.[2–4] Taking into account the differences in properties between a coating and a substrate, TBC systems have gradually developed from single-layer to double- or multilayer systems to improve the bonding strength.[5–7]

On the basis of practical applications, a series of experiments have been carried out on single-, double-, and multilayer coating systems. Zheng et al.[8] investigated ways to achieve stable and efficient combustion of gasoline using compression ignition using a piston with a TBC. Poursaeidi et al.[9] studied the effect that TBCs have on the temperature distribution and fracture of a real GEF9 turbine blade. Texier et al.[10] discussed the tensile behavior of the MCrAlY coating after studying its stress–strain relationship and microstructure. Fritscher et al.[11] evaluated the cyclic lifetime of the TBC system using elemental analysis of the alumina–zirconia mixed zone. Tan et al.[3] explored the wear resistance and fracture toughness of a double-layer WC-CoCr protective coating. Liu et al.[12] studied the thermal shock performance and failure behavior of $Zr_6Ta_2O_{17}$-8YSZ double-ceramic-layer TBCs. Guo et al.[13] evaluated the high-temperature interface stability of a YSH16-YbMS-Si tri-layer TBC system.

In addition to practical applications, corresponding application simulations have been carried out in more depth. Xiao et al.[14] carried out a reliability assessment and lifetime prediction of TBCs on gas turbine blades. Hu et al.[15] simulated the effect that oxidation within

JUNYI XIAO, YU GU, and HAITAO LU are with the College of Electromechanical Engineering, Qingdao University of Science and Technology, Qingdao, 266061, P.R. China. JIAJING PAN is with the College of Electromechanical Engineering, Qingdao University of Science and Technology and also with the Qingte Group Limited Company, Qingdao, 266106, P.R. China. Contact e-mail: panjiajing1234@tju.edu.cn NAN YU and XIAOLIN CHEN are with the Qingte Group Limited Company. MINGLI LV is with the Qingdao Yongzhao New Material Technology Limited Company, Qingdao 266101, P.R. China.

the BC of the TBC system has on residual stress and failure modes around the thermally grown oxides. Cai et al.[16] used numerical simulations to investigate the effect that CaO-MgO-Al$_2$O$_3$-SiO$_2$ penetration has on the stress behavior at the TC–BC interface in the TBC system.

Further, a series of constructive simulations have been developed to clearly demonstrate the particle-spraying behavior. Bobzin et al.[17] investigated the constitutive behavior of the TBC single particle using atmospheric plasma spraying on flat and rough substrate surfaces. Fardan et al.[18] simulated a single-particle impact heat transfer model for YSZ TBC that incorporates the effects of thermal expansion coefficients using a pure Eulerian approach. Lin et al.[19] carried out single- and multi-particle spray simulations and studied the evolution of their residual stress. Song et al.[20] developed a multi-particle cold spraying model and used it to predict coating porosity based on a Coupled-Eulerian–Lagrangian (CEL) analysis. Xiao et al.[21] similarly developed a multi-particle simulation model for plasma spraying that is based on the CEL method.

Admittedly, there are many reports on TBC systems. These range from practical applications to application simulations and from application simulations to constructive simulations. However, the existing construction simulations are mainly focused on single-layer coatings (that are sprayed with single or multiple particles). These are not sufficiently suitable for the spraying conditions of double-layer coating systems. The consideration of presenting the construction simulation that is suitable for the plasma-sprayed ceramic–metal coating stimulates this work.

In this work, plasma spraying has been used to prepare ceramic–metal TBC systems that are commonly used in industry. These include Y$_2$O$_3$-MCrAlY (thermal oxidation resistance), 8YSZ-MCrAlY (thermal conductivity resistance), and Cr$_2$O$_3$-Ni20Cr (thermal corrosion resistance). The main research on these systems is divided into two parts, experiments and simulations. The experimental work is carried out first for coating morphological and structural characterization and then for elemental and coating properties testing. The first is the basis for simulation, and the second serves as a reference for coating properties. The simulation work has two purposes. First, it is performed to validate models, and the second is to explore the forming behavior of the particles and their impact effects on the substrate.

On the basis of the above work, this study presents the development of a simulation model for a plasma-sprayed bilayer system and presents the construction of three different plasma-sprayed ceramic–metal TBC systems. Overall, the work aims to investigate the construction mechanism of plasma-sprayed zceramic–metal TBC systems via the combination of experimental and simulation methods to provide a reasonable reference for constructing similar coatings in industry and to improve the basic reference for the subsequent in-depth study of tri- or multilayer coatings.

II. EXPERIMENT AND SIMULATION

A. Plasma-Spraying Bilayer-Coating System

Plasma-spraying experiments were carried out with a spraying system from Oerlikon Metco, where the plasma gun was a side-fed type (model F4MB-XL) and the powder was a conventional sphere type. The three ceramic–metal TBC systems that were used in the experiments consisted of TC–BC: Y$_2$O$_3$-MCrAlY, 8YSZ-MCrAlY, and Cr$_2$O$_3$-Ni20Cr. Inconel718 was used as the substrate; it is an alloy that is widely used in industrial manufacturing. Before spraying, the substrate was cut into rectangles and preheated to 673 K. The plasma-spraying process and its process parameters are shown in Figure 1 and Table I, respectively.[22]

After spraying, the samples were further cut into small rectangles with dimensions of 10 × 5 × 3 mm. Experimental characterization began with macroscopic morphology, and the microstructure was characterized using a metallurgical microscope at low magnification (×200 and ×500) and a scanning electron microscope (SEM) at high magnification (×2000). In addition, energy-dispersive spectrometry (EDS) was carried out at the TC–BC substrate interface. Finally, the porosity and microhardness were characterized using ImageJ software and a microhardness tester, respectively. The information about the coating characterization is as follows: the metallographic microscope was an FY-MIAS-40MDX, from FUIWIN; the SEM was a JSM-6300, from HITACHI; the EDS was an INCA x-sight, from OXFORD INSTRUMENTS; the version of ImageJ was 1.48, from the American National Institutes of Health; and the microhardness tester was an FY-HV-1000CWZ, from FUIWIN.

B. Spray Simulation of Bilayer-Coating System

The simulation of the bilayer-coating system was based on the following assumptions: (1) The geometry of the particles is an ideal sphere. (2) The impact angle of the particles toward the substrate remains vertical. (3) Both the ceramic and metal particles follow the same particle size distribution law. (4) Before collision, the temperature and velocity of the particles and the substrate remain constant.

Constructing coatings is often accompanied by complex deformation situations, such as large stresses and high stress rates, and these are even more pronounced in the case when plasma spraying is used for bilayer-coating systems. Therefore, the CEL method was chosen for this study. The substrate and particles were set up as Lagrangian parts, and all particles were embedded in an Eulerian part as a reference part. The Euler part and its internal particles were partitioned and gave two material properties. Specifically, the different particles were given different impact speeds and temperatures, and the substrate was fixed and given a certain preheating temperature.

There were 150 simulated particles that contain four particle sizes: 20, 30, 40, and 50 μm. 100 of the particles were used as ceramic TC particles, and 50 were used as
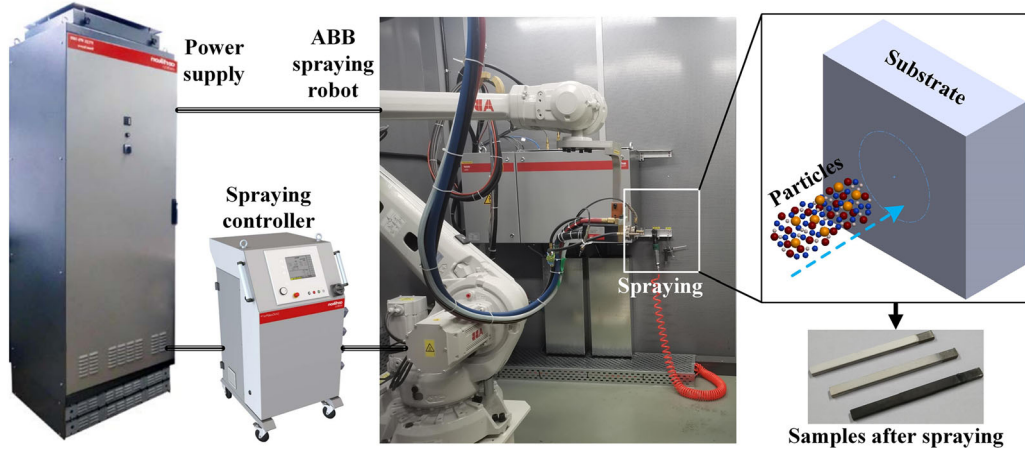
Fig. 1—Plasma-spraying diagram.

Table I.   Plasma-Spraying Process Parameters

Coatings	Ar / NLPM	H$_2$ / NLPM	Arc Current/A	Powder Feed Angle/deg	Powder Feed Rate /g/ mm	Spray Distance / mm	Spray Angle/ deg
Ceramic TC	38	17	600	90	65	120	90
Metal BC	57	11	500	90	20	120	90

metallic BC particles. Each particle followed the same log-normal particle size distribution function[19]:

$$f(d_p) = 50\left[1 + erf\left(\frac{1}{\sqrt{2}\sigma}\ln\left(\frac{d_p}{d_{p,AVG}}\right)\right)\right], \quad [1]$$

where $f(d_p)$ is the cumulative probability distribution of the particle size, d_p is the particle size, $d_{p,AVG}$ is the mean particle size, and the parameter σ is 0.36. According to computational fluid dynamics (CFD), the particle velocity (V_p) and temperature (T_p) can be described using the following motion Eq. [2] and heat transfer Eq. [3]:[23]

$$m_p\frac{dV_p}{dt} = \frac{1}{2}C_D A_P \rho_g V_{rel}^2, \; V_{rel} = V_g - V_p, \quad [2]$$

$$m_p C_p \frac{dT_p}{dt} = S_p h T_{rel}, \quad T_{rel} = T_g - T_p, \quad [3]$$

where m_p is the particle mass, C_D is the drag coefficient (by the classical equation), A_p is the cross-sectional area of the particle perpendicular to the gas flow direction, ρ_g is the gas density, c_p is the specific heat of the particle, S_p is the surface area of the particle, and h is the heat transfer coefficient.[24] Furthermore, V_{rel} and T_{rel} are respectively the relative velocity and relative temperature between the particle and carrier gas.

The Johnson–Cook Constitutive Model, which is applicable for impact testing, was chosen to describe the material properties for the purpose of accurately simulating the dynamic impact processes. The relevant material properties are shown in Table II.[18,25–27]

In Table II, ρ is the mass density, β is the inelastic thermal coefficient, λ is the thermal conductivity, and c is the specific heat. E is the Young modulus, and μ is Poisson's ratio. A is the initial yield stress, B is the hardening modulus. C is the strain rate coefficient, n is the hardening exponent, m is the thermal softening exponent, and $\dot{\varepsilon}_0$ is the reference strain rate. T_m is the melt temperature, and T_r is the room temperature.

The spray simulation model of the bilayer-coating system is shown in Figure 2. Figure 2(a) shows the 3D model, and Figure 2(b) shows the mesh division. Panels (b-1), (b-2), and (b-3) are enlarged views of the corresponding areas in Figure 2(b). The 3D model was created in SOLIDWORKS. The subsequent assembly, meshing, and calculation tasks were carried out in ABAQUS. The rectangle was the Lagrangian part (substrate), and the cylinder was the Eulerian part (embedded with 150 spherical particles). For accurate simulation and efficient calculation, the mesh of the cylinder (b-1) and the impacted side (b-3) of the substrate were refined, and the impacted surface of the substrate was meshed from the inside to outside in a transition from small to large (b-2).

III.   EXPERIMENTAL RESULTS AND DISCUSSIONS

A. *Macromorphology*

The macromorphology of the specimen is shown in Figure 3, and enlarged views of the corresponding ceramic TCs are presented in Figures 3(a), (b), and (c).

Properties			Ceramic TC			Metal BC		Substrate Inconel 718
			8YSZ	Y_2O_3	Cr_2O_3	MCrAlY	Ni20Cr	
General	ρ	kg/m^3	5890	5010	5210	7320	8400	8195
	β	—	0.9	0.9	0.9	0.9	0.9	0.9
	λ	W/m·K	2	2.32	2.7	16.7	16.75	11.4
	c	J/kg·K	713	656	900	764	440	430
Elastic	E	GPa	241	290	340	186	206	200
	μ	—	0.32	0.3	0.25	0.3	0.28	0.3
Plastic	A	MPa	420	401	270	150	180	980
	B	MPa	521	288	200	280	300	1370
	C	—	0.07	0.07	0.025	0.042	0.025	0.02
	n	—	0.184	0.2	0.3	0.141	0.3	0.164
	m	—	0.0197	0.09	1	0.54	1	1.03
	$\dot{\varepsilon}_0$	1/s	0.418	1	1	1	1	1
	T_m	K	2988	2683	2708	1723	1673	1573
	T_r	K	298	298	298	298	298	298
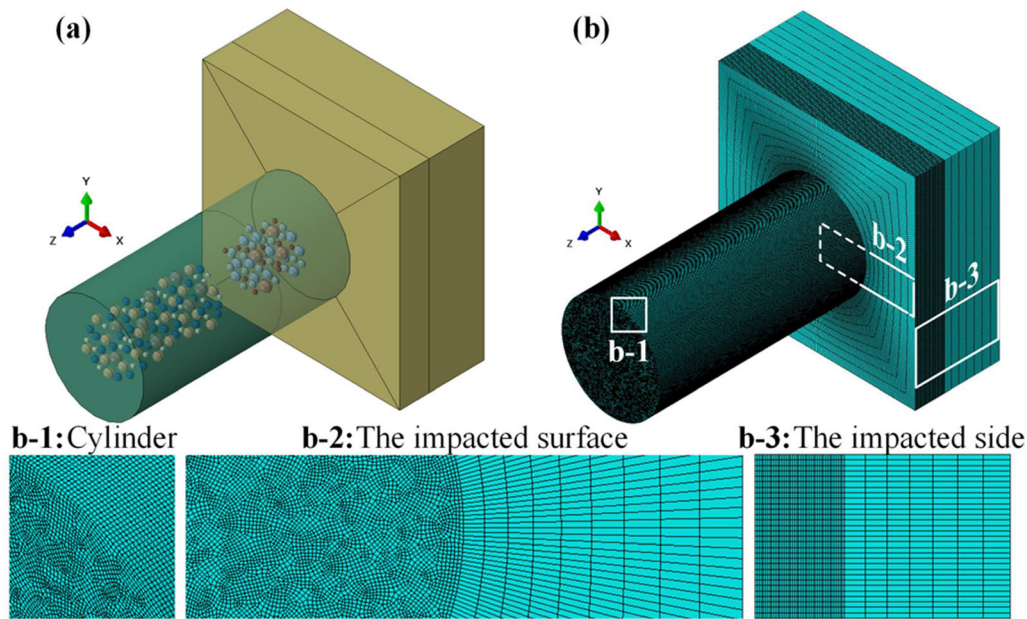
Fig. 2—Simulation model: (*a*) 3D model and (*b*) mesh division.

None of the specimens had visible chips and cracks. The metal BC could not be directly observed because it was covered with TC. The three ceramic TCs had different colors, depending on their material compositions: the Y_2O_3 coating appeared white; the 8YSZ coating appeared light yellow; and the Cr_2O_3 coating appeared dark gray.

B. *Microstructure*

Figure 4 shows the metallographic structure of each coating under low magnification. The approximate thicknesses of the coatings can be seen in Figures 4(a), (d), and (g). As seen in Figures 4(b), (e), and (h), the 8YSZ and Cr_2O_3 coatings had a large number of massive precipitates and cavities compared to the Y_2O_3 coating. As seen in Figures 4(c), (f), and (i), the thickness of the Ni20Cr coating was more stable than that of the MCrAlY coating, and it showed a clear droplets stacking phenomenon. It is inferred that MCrAlY was constructed in the molten state, whereas Ni20Cr was constructed in the semi-molten state.

The microscopic morphology of each coating under high magnification is shown in Figure 5. Panels (a) through (c) show the coating surfaces, and panels (d) through (h) show the coating cross sections. From comparing Figures 5(a), (b), and (c), it is seen that the Y_2O_3 particles were spread in a pie shape with splashing of tiny molten droplets. The 8YSZ particles showed a crater shape and a pie shape. The Cr_2O_3 particles were
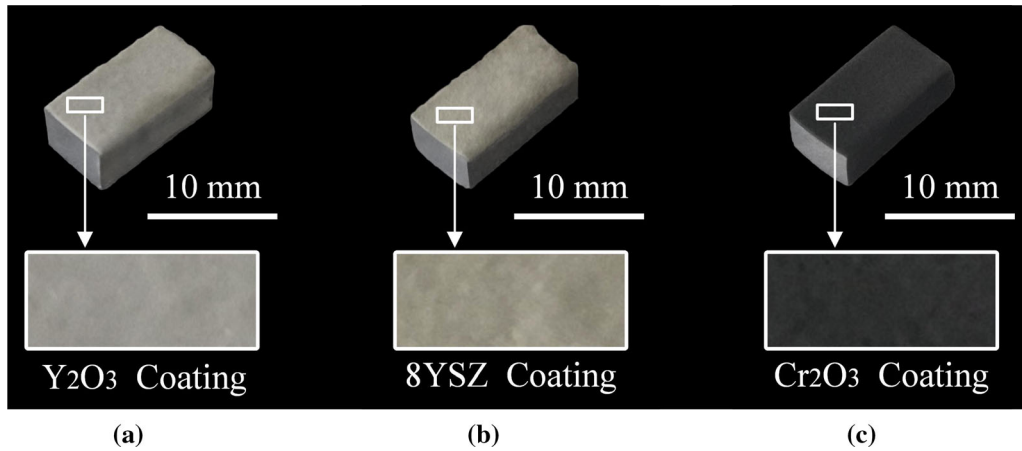
Fig. 3—Macromorphology of the coatings: (*a*) Y_2O_3-MCrAlY coating, (*b*) 8YSZ-MCrAlY coating, and (*c*) Cr_2O_3-Ni20Cr coating.

mostly hill shaped with obvious stacking. It is. therefore, inferred that the Y_2O_3 and 8YSZ coatings have a higher degree of melting and lower porosity than the Cr_2O_3 coatings. As seen in Figures 5(d), (e), and (f), the 8YSZ and Cr_2O_3 coatings were significantly more porous than the Y_2O_3 coating. 8YSZ coating cavities were large and concentrated, whereas Cr_2O_3 coating cavities were small and dispersed. As seen in Figures 5(g) and (h), the Ni20Cr coating was dispersed with a large number of tiny cavities and had a clear stacking texture compared to the MCrAlY coating. This is consistent with the speculation made regarding Figure 4, specifically that Ni20Cr was constructed in a semi-molten stacking state.

C. *Element Distribution*

Figure 6 shows the cross-sectional element distributions of the bilayer-coating system. The characteristic elements (Y, Al, Zr, O, and Nb) of each coating are marked according to their chemical compositions. To assist in the analysis, the common elements (Ni and Cr) in the substrate and BC are marked. The characteristic elements (Mo) in the substrate are also marked.

As seen in Figures 6(b), (d), and (f), Y, Zr, and O were clearly enriched in TC, Al was clearly enriched in BC, and Nb was clearly enriched in the substrate. There was no clear diffusion of any of these five elements. As seen in panels (b-1), (b-2), (d-1), and (d-2), Ni and Cr were enriched in the substrate and BC. As seen in panels (f-1) and (f-2), Ni was enriched in the substrate and BC. In contrast, Cr was enriched throughout the cross section. As seen in panels (b-3), (d-3), and (f-3), Mo was enriched in the substrate and showed significant diffusion into the coating. The above phenomenon shows that the bonding of the TC–BC substrate was a combination of mechanical and metallurgical bonding. Specifically, the diffusion of ceramic TC to metal BC was weak, whereas the diffusion of the substrate to metal BC was more obvious. Therefore, it is inferred that the metallurgical bonding of substrate BC was more significant and had a higher bond strength than TC–BC.

D. *Coating Porosity*

The porosity of the three bilayer-coating systems is shown in Figure 7. Considering that the depth of field of the metallographic microscope is much smaller than that of the SEM, the measurements that are based on the metallographic structure are considered to be larger values, whereas the measurements that are based on the SEM morphology are considered to be smaller values. Among the TCs, the Y_2O_3 coating had the lowest porosity (1 to 3 pct), and the 8YSZ and Cr_2O_3 coatings had a higher porosity of 10 to 16 pct and 12 to 17 pct, respectively. Among the BCs, the porosity of the MCrAlY coating was low (1 to 2 pct), whereas the Ni20Cr coating was relatively high (3 to 7 pct). From both Figures 4 and 5, it is presumed that the stacking in the semi-molten state (Cr_2O_3 and Ni20Cr coatings) was more prone to more porosity.

There are differences in porosity between TC and BC in the three TBC systems. The smallest difference appeared in the Y_2O_3-MCrAlY TBC system, followed by the 8YSZ-MCrAlY TBC system; the largest difference was in the Cr_2O_3-Ni20Cr TBC system. According to these differences in porosity properties, the bonding strengths of the three TBC systems are presumed to be (in descending order) Y_2O_3-MCrAlY, 8YSZ-MCrAlY, and Cr_2O_3-Ni20Cr.

E. *Coating Microhardness*

Sections of each coating were subjected to 10 microhardness tests, and the results are shown in Figure 8. The corresponding average microhardness values are shown in Table III. The microhardness of the TCs is shown in descending order, which is as follows: Cr_2O_3, 8YSZ, and Y_2O_3. The average microhardness values were 1007.15 $HV_{0.5}$, 730.27 $HV_{0.5}$, and 478.69 $HV_{0.5}$, respectively. Among the BCs, the microhardness of the Ni20Cr coating was slightly higher than that of the MCrAlY coating with average microhardness values of 320.77 $HV_{0.5}$ and 280.54 $HV_{0.5}$, respectively. In conjunction with Figure 7, the Y_2O_3, MCrAlY, and Ni20Cr coatings do not have high microhardness because of
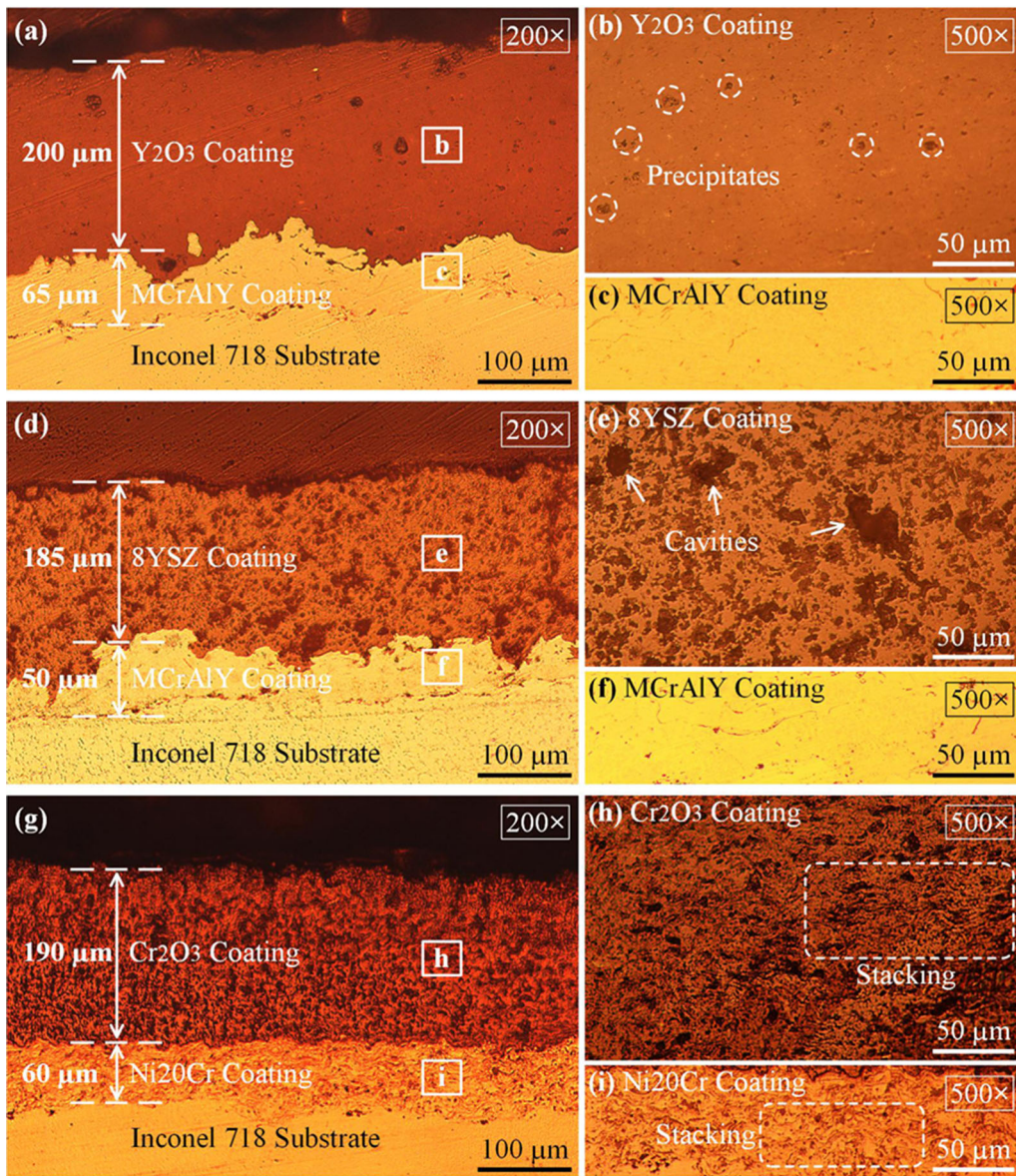
Fig. 4—Metallographic structure of the coatings under low magnification: (*a*) through (*c*) Y_2O_3-MCrAlY coating, (*d*) through (*f*) 8YSZ-MCrAlY coating, and (*g*) through (*i*) Cr_2O_3-Ni20Cr coating.

lower porosity; however, the YSZ and Cr_2O_3 coatings are the opposite of the first three coatings. Thus, the effect of porosity on the coating microhardness is not significant. It is presumed that more significant influencing factors exist, such as the precipitated phase of the coatings.

From comparing the microhardness differences between TC and BC in the three TBC systems, it can be seen that the Y_2O_3-MCrAlY TBC system has the smallest difference, followed by the 8YSZ-MCrAlY TBC system; the Cr_2O_3-Ni20Cr TBC system has the largest difference. On the basis of the differences in microhardness properties, the bonding strengths of the three TBC systems are presumed to be (in descending order) Y_2O_3-MCrAlY, 8YSZ-MCrAlY, and Cr_2O_3-Ni20Cr. This is consistent with the above presumptions that are based on the differences in porosity properties.

IV. SIMULATION AND ANALYSIS

A. Model Verification

The construction process of the plasma-sprayed bilayer-coating system is shown in Figure 9 (from top to bottom: the Y_2O_3-MCrAlY coating, 8YSZ-MCrAlY coating, and Cr_2O_3-Ni20Cr coating). The initial and end times for each metal BC were 600 ns and 1400 ns. The initial and end times for each ceramic TC were 2400 ns and 4800 ns. As the spraying progresses, the particles of each coating spread out, and their strain became increasingly different.

Simulated and experimental droplet spreading strains were compared to verify the reasonableness and feasibility of the simulation. The top half of Figure 10 shows the top view of the simulation, and the bottom half of the figure shows the microscopic morphology. A
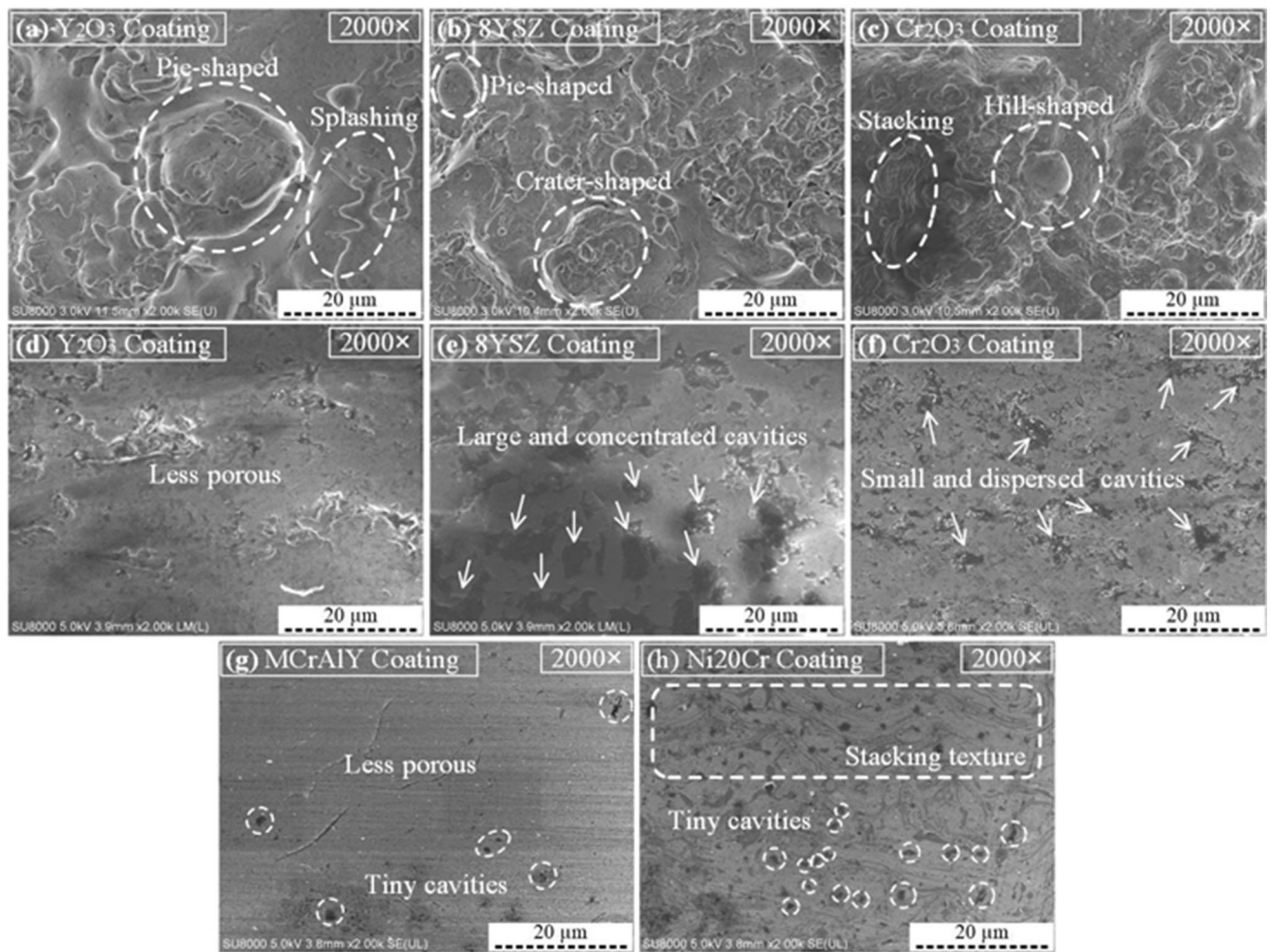
Fig. 5—Microscopic morphologies of the coatings under high magnification: (*a*) through (*c*) surfaces and (*d*) through (*h*) cross sections.

comparison of the top and bottom shows that the actual spreading of the coating droplets was consistent with the simulation results. Y_2O_3 particles were mostly constructed in a circular pie shape with a flat center. 8YSZ particles were mostly constructed in a crater shape with a depressed center. Cr_2O_3 particles were mostly constructed in a hill shape with a raised center.

From the combination of Figures 9 and 10, it is seen that the 8YSZ-MCrAlY coating had the highest strain, followed by the Y_2O_3-MCrAlY coating. The Cr_2O_3-zNi20Cr coating was the smallest. The strain of the coating is presumed to be related to the softening degree. 8YSZ particles formed a crater-shaped structure (which was prone to higher strains) as a result of more complete softening occurring. Y_2O_3 particles formed a pie-shaped structure (lower strains) because there was moderate softening, and Cr_2O_3 particles formed a hill-shaped structure (lowest strains) because there was minimal softening.

B. *Forming Behavior of Particles*

Figure 11 shows the temperature change during particle impact in bilayer-coating systems. For each

coating, the differences in the process parameters (Table I) resulted in relatively lower temperatures for the BC than for the TC. There was little difference in particle temperature between the two BCs (about 1400 K to 1800 K), whereas the three TCs (8YSZ, Y_2O_3, and Cr_2O_3) had sequentially higher particle temperatures (about 1800 K, 1900 K, and 2150 K, respectively). Combined with Figure 9, it is found that the particle temperatures of 8YSZ and Y_2O_3 were lower than those of Cr_2O_3, but both had a higher thermal softening degree than Cr_2O_3. As a result, temperature differences resulted from differences in thermal conductivity (λ in Table II), and softening degree differences resulted from differences in the thermal softening exponent (m in Table II). For the bilayer-coating system, the overall temperatures of the Y_2O_3-MCrAlY, 8YSZ-MCrAlY, and Cr_2O_3-Ni20Cr systems were significantly influenced by the corresponding TCs. Therefore, during the overall construction of the three bilayer-coating systems, the construction of the TC was the main factor that caused the temperature effects compared to the construction of the BC.

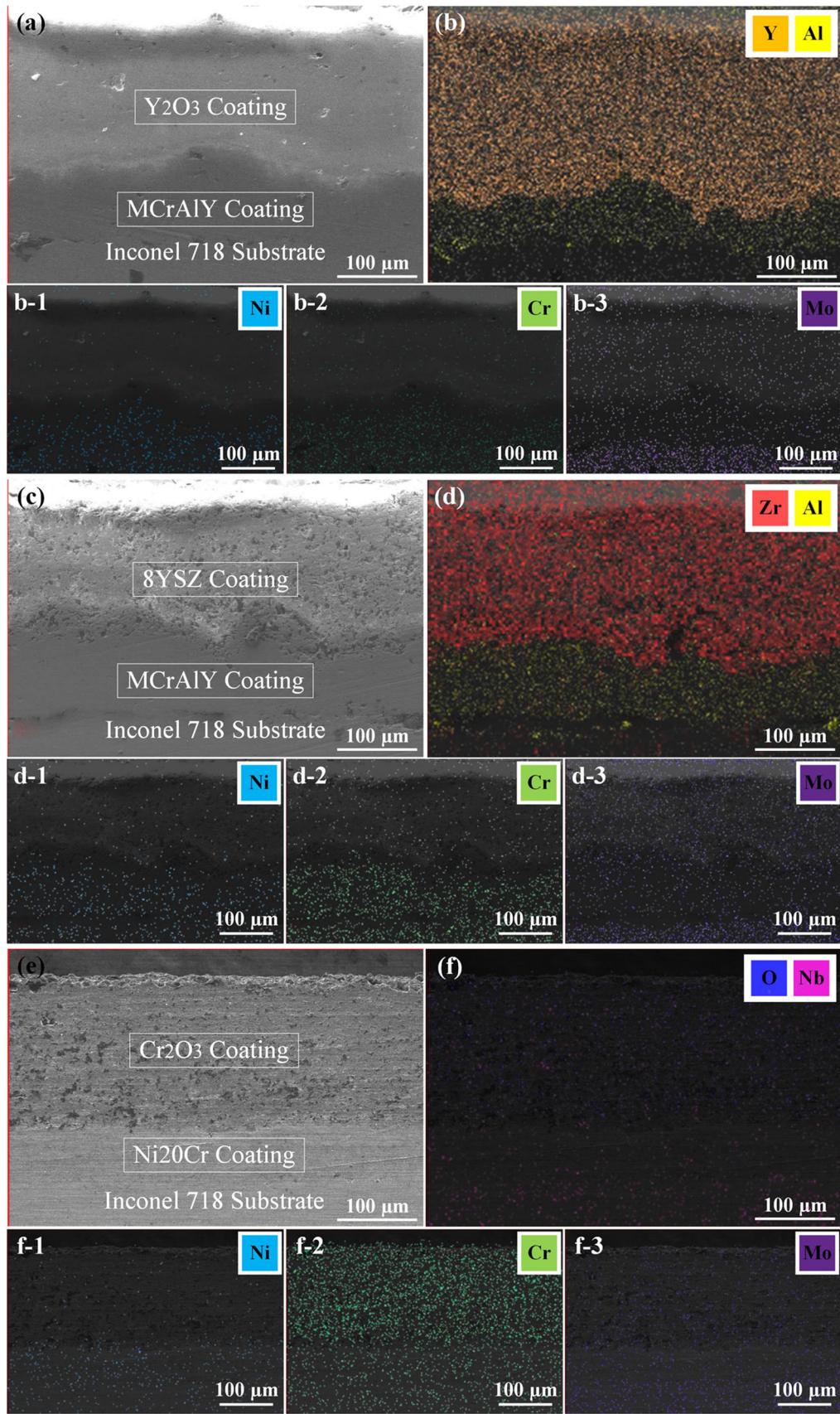Figure 12 presents changes in the equivalent stress during particle impact for the bilayer-coating systems.

Fig. 6—Distribution of elements in the cross section of the coatings: (*a*) and (*b*) Y_2O_3-MCrAlY coating, (*c*) and (*d*) 8YSZ-MCrAlY coating, and (*e*) and (*f*) Cr_2O_3-Ni20Cr coating.
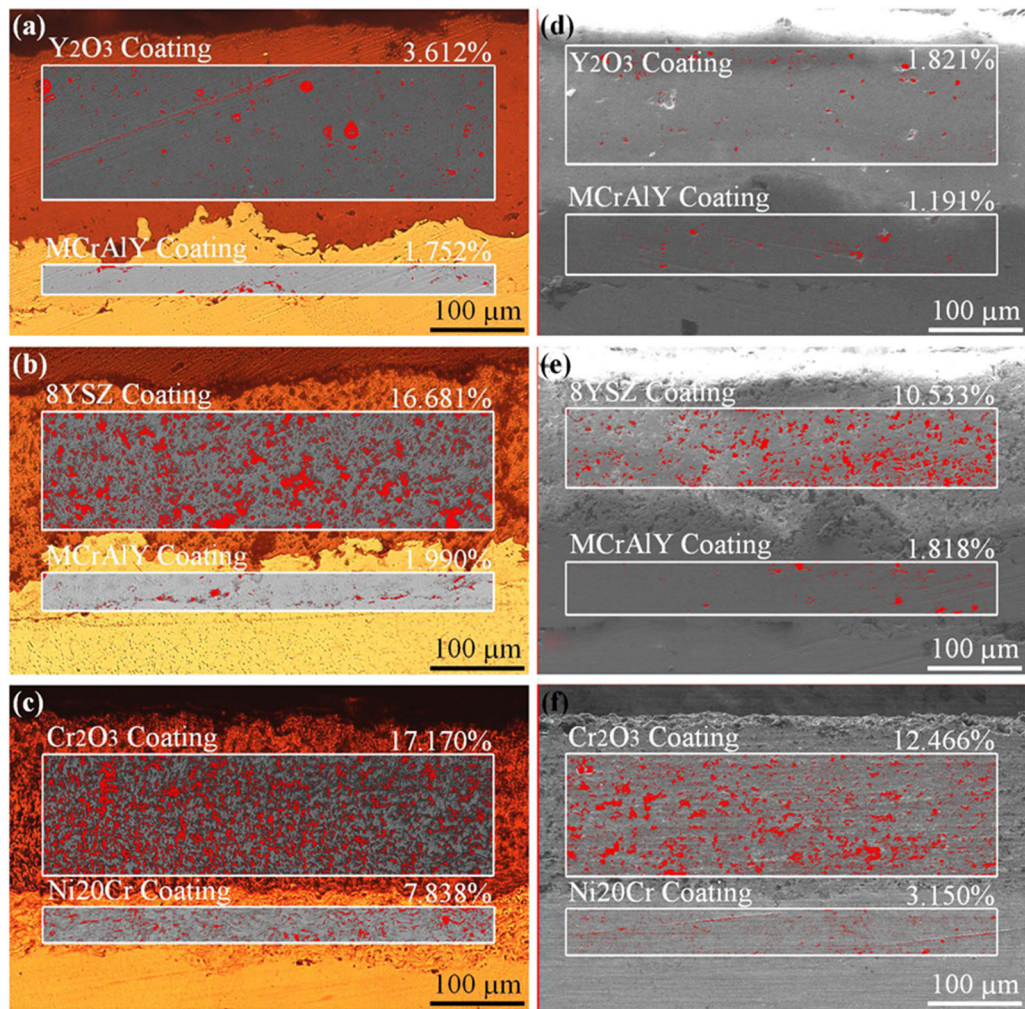
Fig. 7—Coating porosity: (*a*) through (*c*) based on metallographic structures and (*d*) through (*f*) based on SEM morphologies.

For each coating, the equivalent stress of the MCrAlY particles was lower (around 50 MPa), whereas that of the Ni20Cr particles was higher (around 100 MPa). In addition, the descending order of equivalent stresses for the TC particles is Cr_2O_3 (around 75 MPa), Y_2O_3 (around 50 MPa), and 8YSZ (around 25 MPa). This trend was the opposite of the trend for the strain (Figure 9). Specifically, when the strain of the particle was lower, the equivalent stress of the particle was higher because of impact. It is, therefore, inferred that the equivalent stress of the particle was related to the softening degree; that is, particles with a low softening degree (Cr_2O_3) tended to generate higher equivalent stresses on impact. For the bilayer-coating system, the equivalent stress was generated by the impact of the particles, and the BC particles generated a relatively higher equivalent stress than the TC particles. The overall equivalent stresses of the Y_2O_3-MCrAlY, 8YSZ-MCrAlY, and Cr_2O_3-Ni20Cr systems were significantly influenced by the corresponding BCs.

Therefore, during the overall construction of the three bilayer-coating systems, the construction of the BC was the main factor that caused the equivalent stress effects compared to the construction of the TC.

C. *Impact Effects on Substrates*

Figure 13 shows the temperature change of the substrate during the construction of three bilayer-coating systems. The substrate had a basic temperature of 660 K to 675 K because of the preheating process. At 600 ns, the substrate produced a number of small circular high-temperature zones as a result of the impact of high-temperature particles. At 1400 ns, the high-temperature zone was significantly larger, and the temperature increased. At 2400 ns and 4800 ns, the temperature of the high-temperature zone decreased, and the area increased slightly. By comparison, the substrate was subjected to higher temperatures that were generated by the impact of Cr_2O_3-Ni20Cr particles,
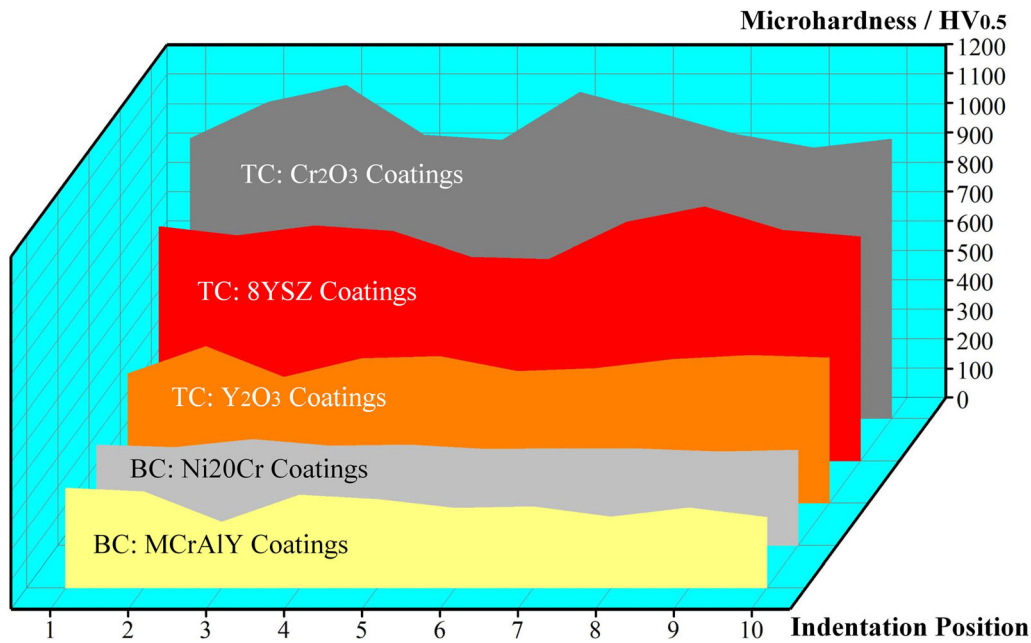
Fig. 8—Microhardness of each coating.

Table III. Average Microhardness Values for Each Coating

Indentation Position	Cr$_2$O$_3$	8YSZ	Y$_2$O$_3$	Ni20Cr	MCrAlY
Average Microhardness (HV$_{0.5}$)	1007.15	730.27	478.69	320.77	280.54

whereas lower temperatures were generated by the impact of Y$_2$O$_3$-MCrAlY and 8YSZ-MCrAlY particles. Combined with Figure 11, it is presumed that the lower BC softening easily leads to higher temperatures on the substrate when it is impacted by the bilayer-coating particles. In addition, the BCs that are constructed first protect the substrate and reduce the effect of the TCs.

Figure 14 shows the equivalent stress change of the substrate during the construction of three bilayer-coating systems. The impact created a stress zone that consisted of a number of small circular stress zones in the center of the substrate. The stresses in each of the small circular stress zones ranged from approximately 350 to 560 MPa; the stresses began at 600 ns, increased at 1400 ns, and did not change much at 2400 ns and 4800 ns. At 600 ns, the BC particles impacted the substrate and spread the microstress around each small circular stress zone. At 1400 ns, the microstress disappeared. At 2400 ns, the TCs impacted the substrate and generated microstress again. At 4800 ns, the microstress disappeared. By comparison, the impact stresses of the Ni20Cr particles were slightly higher than that of the MCrAlY particles (600 ns and 1400 ns) with a stress concentration of approximately 770 MPa in the center of each small circular stress zone and a more significant

diffusion of microstresses. However, the impact of the Y$_2$O$_3$, 8YSZ, and Cr$_2$O$_3$ particles did not cause large stress effects on the substrate (at 2400 ns and 4800 ns), and this again demonstrates the protective effect of BCs on the substrate. This also indicates that when the substrate is impacted by the bilayer-coating particles, the substrate stress is mainly related to the softening degree of the BC particles, whereas the less softened Ni20Cr particles tend to have a higher impact stress.

V. CONCLUSIONS

Three bilayer-coating systems (Y$_2$O$_3$-MCrAlY, 8YSZ-MCrAlY, and Cr$_2$O$_3$-Ni20Cr) were constructed on the Inconel718 substrate by a plasma-spraying process. Experiments were carried out to characterize the macroscopic morphology, microstructure, and elemental distributions and to measure the coating porosity and microhardness. In addition, a simulation model of the plasma-sprayed bilayer system was constructed and verified. The constructive behavior of particles and substrates was explored for the impact process of plasma-sprayed bilayer-coating systems. The following conclusions are drawn from this research:
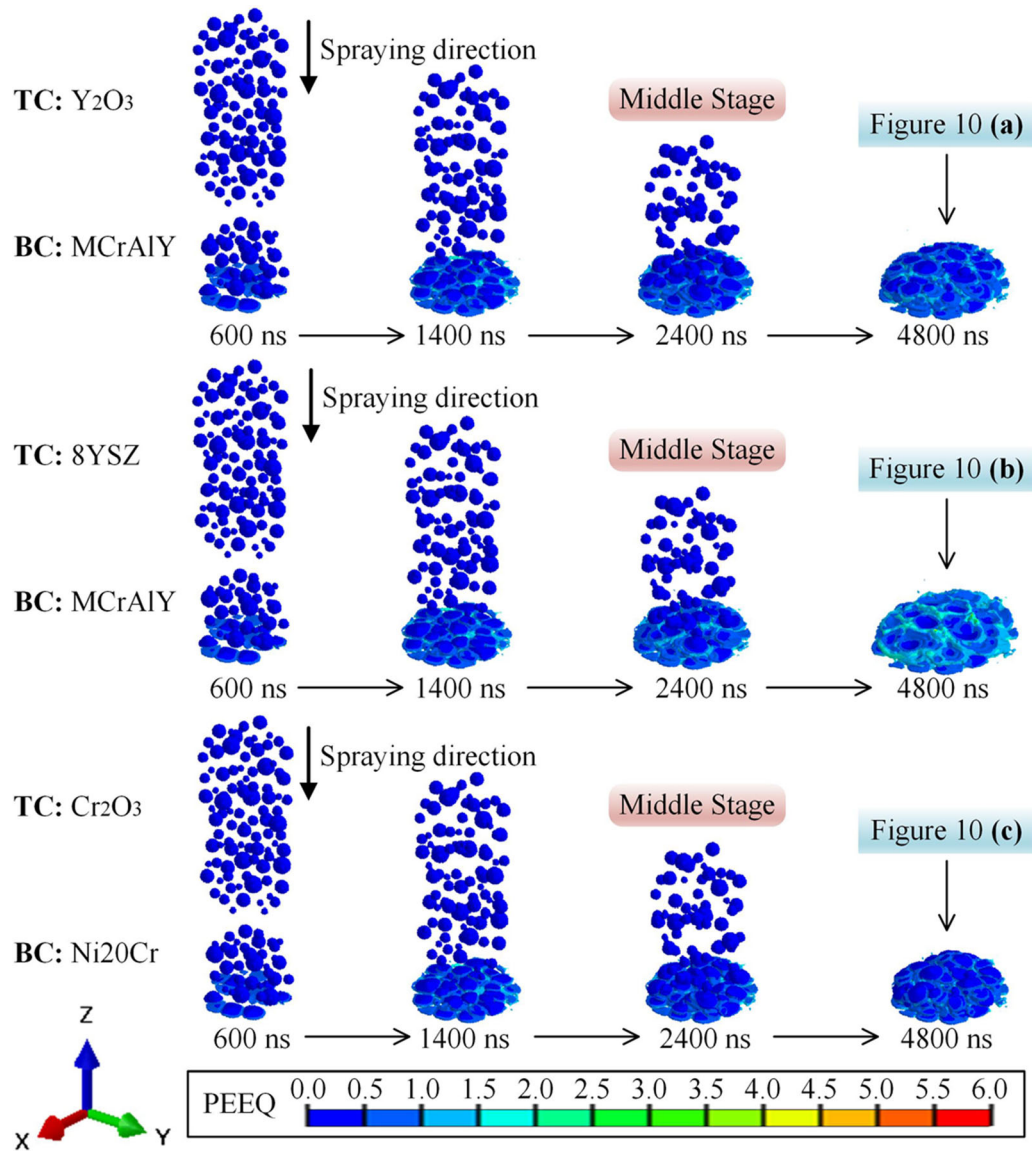
Fig. 9—Construction of the bilayer-coating system.

(1) Each coating has a different morphology as a result of the different degrees of softening. Specifically, MCrAlY coatings are constructed in a molten state, whereas Ni20Cr is constructed in a semi-molten stack. Y_2O_3 coatings are spread in a pie shape, 8YSZ coatings have a crater shape, and Cr_2O_3 coatings are stacked in hill-shaped droplets.

(2) The bonding of the TC–BC substrate is both mechanical and metallurgical. The elemental diffusion of TC–BC is significantly weaker than that of the substrate BC. This indicates that the substrate BC has a higher bond strength than TC–BC because of how it easily achieves a higher metallurgical bond.

(3) The porosity and microhardness of the BCs are lower than those of the TCs. The porosity and microhardness of each coating are in the following order (from highest to lowest): Cr_2O_3, 8YSZ, Y_2O_3, Ni20Cr, and MCrAlY. In the three TBC systems, the property differences between BC and TC are (from largest to smallest) Cr_2O_3-Ni20Cr, 8YSZ-MCrAlY, and Y_2O_3-MCrAlY. It is presumed that the differences in this property affect the bonding strength of the TBC systems and that this results in the order from largest to smallest bonding strength of the three TBC systems: Y_2O_3-MCrAlY, 8YSZ-MCrAlY, and Cr_2O_3-Ni20Cr.

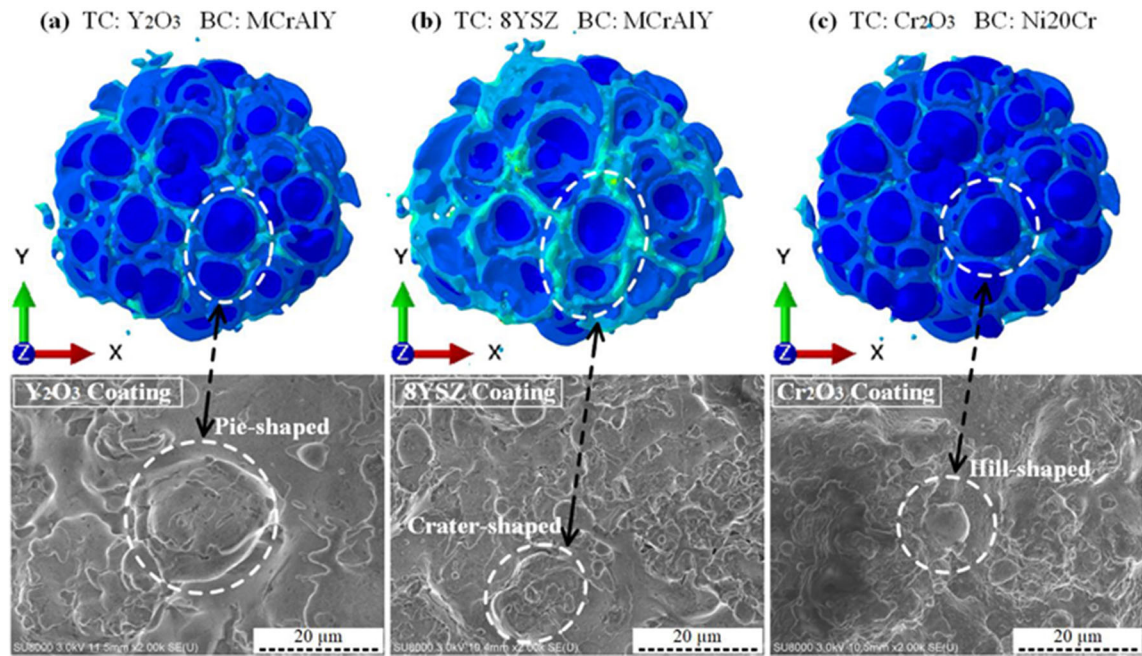(4) The differences in temperature for the particles during impact are related to the differences in
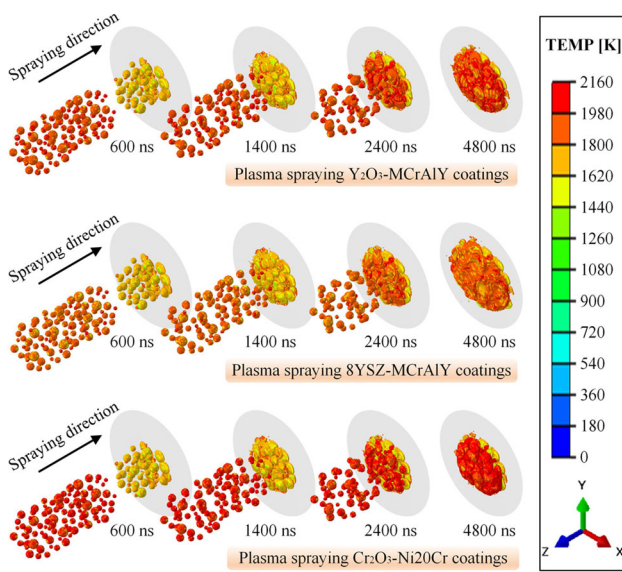
Fig. 10—Verification of droplet strain.

Fig. 11—Temperature changes during particle impact in bilayer-coating systems.

Fig. 12—Equivalent stress changes during particle impact in bilayer-coating systems.

their thermal conductivity. The equivalent stress of the particles is related to their degree of softening, whereas the differences in the degree of melting are related to the thermal softening coefficient. This results in TC particles with significantly higher temperatures than BC but significantly lower equivalent stresses than BC. Therefore, in constructing bilayer-coating systems, the construction of the TC is the main factor that causes the temperature effects, and the construction of the BC is the main factor that causes the equivalent stress effects.

(5) The high-temperature zones and high-stress zones that result from the impact on the substrate were mainly from the BC particles. It is inferred that the BCs that were constructed first protected the
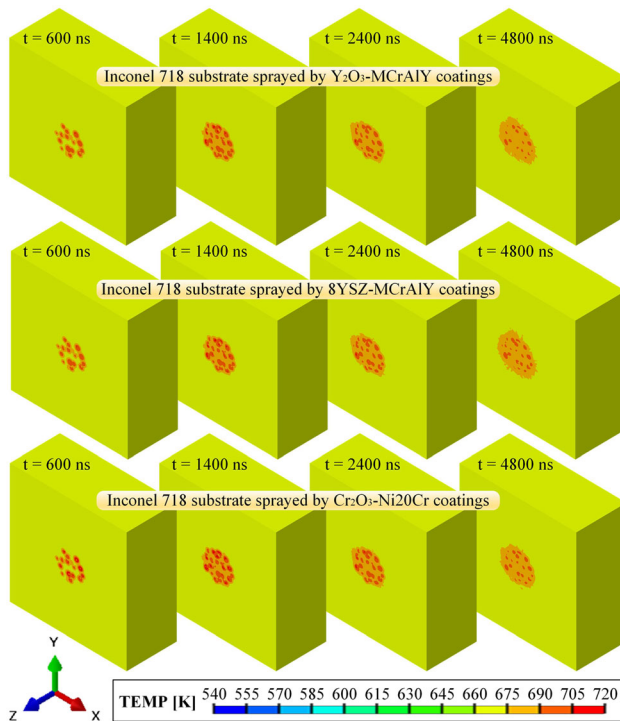
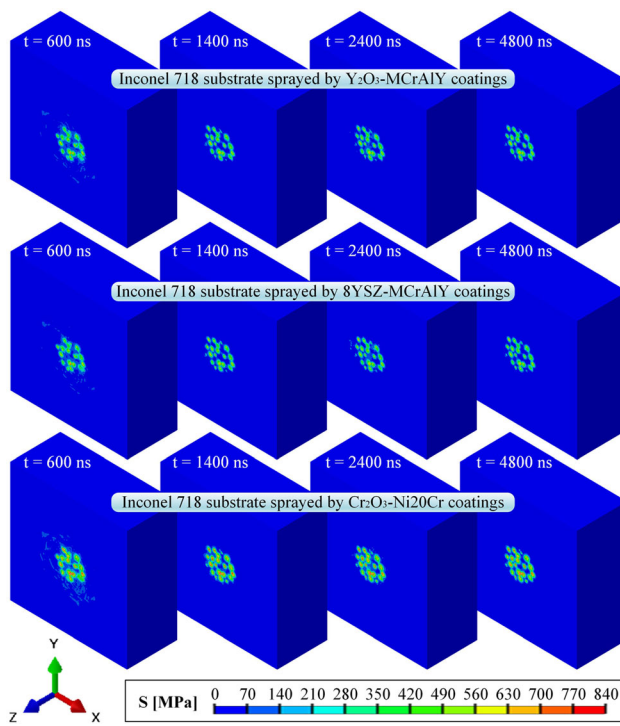Fig. 13—Temperature changes of the substrate by impact.

Fig. 14—Equivalent stress changes of the substrate by impact.

substrate in the subsequent spraying process and reduced the impact effects of the TCs that were constructed later.

CONFLICT OF INTEREST

On behalf of all of the authors, the corresponding author states that there is no conflict of interest.

REFERENCES

1. Z.-Y. Wei, G.-H. Meng, L. Chen, G.-R. Li, M.-J. Liu, W.-X. Zhang, L.-N. Zhao, Q. Zhang, X.-D. Zhang, C.-L. Wan, Z.-X. Qu, L. Chen, J. Feng, L. Liu, H. Dong, Z.-B. Bao, X.-F. Zhao, X.-F. Zhang, L. Guo, L. Wang, B. Cheng, W.-W. Zhang, P.-Y. Xu, G.-J. Yang, H.-N. Cai, H. Cui, Y. Wang, F.-X. Ye, Z. Ma, W. Pan, M. Liu, K.-S. Zhou, and C.-J. Li: *J. Adv. Ceram.*, 2022, vol. 11, pp. 985–1068.
2. K. Mondal, L. Nuñez, C.M. Downey, and I.J. van Rooyen: *Ind. Eng. Chem. Res.*, 2021, vol. 60, pp. 6061–77.
3. X. Tan, J. zhang, H. Zhu, Z. Zhang, X. Zhu, W. Ni, T. Li, T. Kuang, H. Dai and X. Zhang: *Ceram. Int.* 2022, vol. 48, pp. 33992–98.
4. J. Ahn, B. Hwang, E.P. Song, S. Lee, and N.J. Kim: *Metall. Mater. Trans. A.*, 2006, vol. 37, pp. 1851–61.
5. P.G. Lashmi, P.V. Ananthapadmanabhan, G. Unnikrishnan, and S.T. Aruna: *J. Eur. Ceram. Soc.*, 2020, vol. 40, pp. 2731–45.
6. N.P. Padture, M. Gell, and E.H. Jordan: *Science*, 2002, vol. 296, pp. 280–84.
7. L. Wang, D.C. Li, J.S. Yang, F. Shao, X.H. Zhong, H.Y. Zhao, K. Yang, S.Y. Tao, and Y. Wang: *J. Eur. Ceram. Soc.*, 2016, vol. 36, pp. 1313–31.
8. Z. Zheng, P. Chen, F. Zhang, M. Yao, H. Wang, and H. Liu: *Appl. Therm. Eng.*, 2022, vol. 217, 119068.
9. E. Poursaeidi, A. Azizi Far, J. Rahimi and M. R. Javadi Sigaroodi: *Engineering Failure Analysis* 2022, vol. 141, p. 106682.
10. D. Texier, C. Cadet, T. Straub, C. Eberl, and V. Maurel: *Metall. Mater. Trans. A.*, 2020, vol. 51A, pp. 2766–77.
11. K. Fritscher, W. Braue, and U. Schulz: *Metall. Mater. Trans. A.*, 2013, vol. 44A, pp. 2070–82.
12. Q. Liu, X.P. Hu, W. Zhu, G.L. Liu, J.W. Guo, and J. Bin: *Ceram. Int.*, 2022, vol. 48, pp. 24402–10.
13. Q. Guo, W. He, C. Li, J. He, J. Sun, and H. Guo: *Ceram. Int.*, 2022, vol. 48, pp. 9313–23.
14. Y.Q. Xiao, Z.Y. Liu, W. Zhu, and X.M. Peng: *Surf. Coat. Technol.*, 2021, vol. 423, 127572.
15. Z.C. Hu, L. Wang, M.X. Zhuang, H.Y. Zhang, G.S. Li, Y. Liu, Y. Wang, and Y. Yang: *Ceram. Int.*, 2021, vol. 47, pp. 5364–73.
16. Z. Cai, Z. Zhang, Y. Liu, X. Zhao, and W. Wang: *Chin. J. Mech. Eng.*, 2021, vol. 34, p. 128.
17. K. Bobzin, N. Bagcivan, D. Parkot, and I. Petković: *Surf. Coat. Technol.*, 2010, vol. 204, pp. 1211–15.
18. A. Fardan and R. Ahmed: *J. Therm. Spray Technol.*, 2019, vol. 28, pp. 717–36.
19. E. Lin, Q. Chen, O.C. Ozdemir, V.K. Champagne, and S. Müftü: *J. Therm. Spray Technol.*, 2019, vol. 28, pp. 472–83.
20. X. Song, K.L. Ng, J.M.-K. Chea, W. Sun, A.W.-Y. Tan, W. Zhai, F. Li, I. Marinescu, and E. Liu: *Surf. Coat. Technol.*, 2020, vol. 385, 125433.
21. J. Xiao, J. Pan, H. Guo, and M. Lv: *Int. J. Adv. Manuf. Technol.*, 2022, vol. 120, pp. 6393–405.
22. S. Tailor, R.M. Mohanty, and A.V. Doub: *Mater. Today*, 2016, vol. 3, pp. 2725–34.
23. X. Gao, C. Li, D. Zhang, H. Gao, and X. Han: *Surf. Coat. Technol.*, 2021, vol. 405, 126588.
24. J. Pan, S. Hu, L. Yang, K. Ding, and B. Ma: *Mater. Des.*, 2016, vol. 96, pp. 370–76.

25. A. Kiran Kumar and P. Venkataramaiah: *Mater. Today* 2019, vol. 18, pp. 4531–36.
26. Z. Zhu, S. Kamnis, and S. Gu: *Acta Mater.*, 2015, vol. 90, pp. 77–87.
27. K.A. Khor and Y.W. Gu: *Mater. Sci. Eng. A*, 2000, vol. 277, pp. 64–76.